Journal of Physics D: Applied Physics

Study of optical, thermal and radio frequency properties of low emissivity coatings with frequency selective surfaces.

Study of optical, thermal and radio frequency properties of low emissivity coatings with frequency selective surfaces.

R. Alcaín[1,3], E. Carretero[2,3], R. Chueca[1,3], C. Heras[1,3], I. Salinas[1,3]

[1]Departamento de Ingeniería Electrónica y Comunicaciones, Universidad de Zaragoza, C/ Maria de Luna, 1, 50018, Zaragoza, Spain

[2]Applied Physics Department, University of Zaragoza, C/Pedro Cerbuna, 12, 50009 Zaragoza, Spain

[3]Grupo de Tecnologías Fotónicas, Instituto de Investigación en Ingeniería de Aragón (I3A), Universidad de Zaragoza, Zaragoza, Spain

Corresponding author: R. Alcaín, ras@unizar.es

Abstract

The use of frequency selective surfaces defined on railcar windows with a metallic low-e coating to improve the reception of mobile communications signals is becoming ever more common. The proximity of the glass to the passenger in this scenario has introduced a new parameter to consider, aesthetics. This paper presents a complete study of the development of a FSS defined by laser ablation, considering all current requirements. The fabricated samples will be characterized in the optical and radiofrequency ranges of the spectrum. Also, by means of an electron microscope, the chemical elements of each area of the samples will be quantified, in order to study the ablation process.

New samples will be made using these parameters, and its performance according to specifications verified. These data will be correlated, using digital image processing, to the aesthetic impact of the engraved FSS, as confirmation of the optimal laser configuration.

Highlights

Analysis of laser ablation on low-e glass.

Visual optimization of frequency selective surfaces over low-e glass.

Radio frequency attenuation of coatings on glass for architecture and transport.

Analysis FSS.

1. Introduction

For years, energy efficient technology has been increasing its relevance in architecture[1][2]. In this field, the most important passive energy source is the sun irradiation. Because of that, the focus is on the modification of the building glazing in order to control both infrared (thermal) and visible sun radiation. This control is obtained by deposition over the glass of different materials in nanometric layers [3], some of them metallic[4][5][6]. These layers can work as interferometric filters, which can be tuned to the desired wavelengths. For instance, a filter can be designed to block infrared light and the heat it transmits while maintaining high transmittance for visible light. Depending on the location of the deposited metallic layers, these advanced glasses can attenuate infrared light in a hot climate (solar control glass) or prevent thermal losses in cold weather (low emissivity glass)[7][8][9].

This technology and the comfort it provides has been applied to different means of transport, especially trains and trams. However, as the metal layers also attenuate electromagnetic signals with frequencies lower than infrared light, this affects the signals increasingly used in mobile technologies. Among these signals, the most relevant are those of mobile communication in the range of 900 to 2600MHz, up to the 5GHz band.

Frequency selective surfaces (FSS) are a solution to this problem. The fundamentals of this technology have been widely discussed, both theoretically and through simulations[10][11]. FSS consist of periodic structures, most of them metallic, which act as frequency filters with features depending on the shape and size of their elements. As stated previously, low-emissive coatings have thin conductive metallic layers, usually silver, which attenuate radio frequencies. Removing such conductive layers from the coating would make it impossible to achieve coatings with adequate photoenergetic properties [12]. The partial elimination of the coating with suitable patterns generates the FSS that allow to preserve the photoenergetic properties while reducing the attenuation of radio frequencies.

In this work, we are going to use a simple FSS design, a grid defined by removing fine parallel lines from the metallic layer. The width and separation of these lines will determine the frequency range of the electromagnetic waves, which will be rejected or allowed to pass. These patterns are engraved on the metallic layer by a laser beam.

There are several studies detailing the use of this technology in low-e glasses and many other applications [13]. However, the use of FSS in low-e glasses still presents a series of unsolved problems, such as the aesthetic aspect. In addition, these existing studies generally study a part of the FSS in isolation: radiofrequency, laser ablation, etc, whereas we intend to study several of these aspects at the same time.

This research addresses the laser ablation of the multilayer, how it affects the glass surface and its characteristics in the visible range, the transparency, and the appearance of the final product[14][15][16]. Our aim is to obtain a FSS as imperceptible as possible to the human eye. We will also study the impact of this treatment on the photo-energetic properties of the low-emissivity layer.

2. Material and methods

2.1 Coatings

The first part of this work will be to fabricate the solar control coating structure. There are many different coatings for solar control and low emissivity glass[17][18], but in this work, we will choose a double silver layer (Fig.1). This composition offers a contrast between the bare glass and the coating, which is visible to the naked eye.

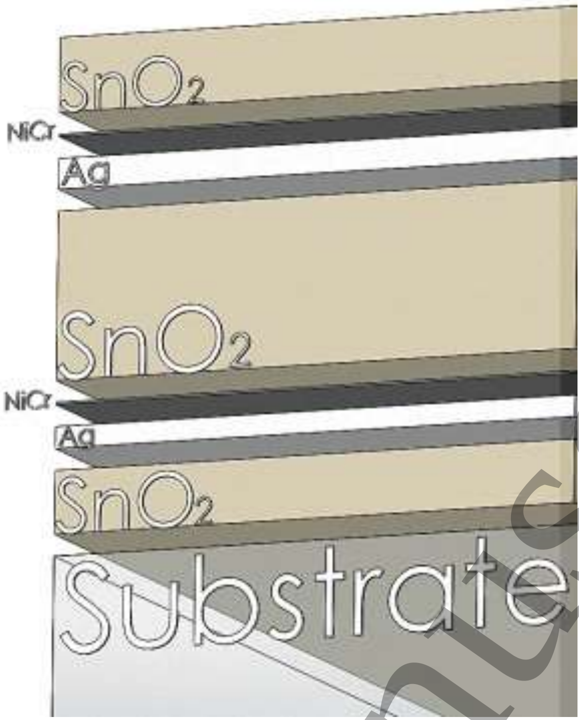

Figure 1: Double silver Low emissive coating (Dag66).

The double silver coating is deposited in a semi-industrial DC pulse high vacuum magnetron sputtering system, using 12 mm thick 600x100mm rectangular cathode targets. This process is similar to those used in large-area industrial applications. The samples are 4mm thick glass (Pilkington Optiwhite), 300x300mm in size. This glass has low optical absorption, which makes it appropriate for optical measurements [19]. Thin multilayers are grown with a base pressure of $2.0x10^{-6}$mbar and a working pressure in the range of 10^{-3}mbar. Note that a pressure of $1.8x10^{-3}$mbar equals a gas flow of 200sccm in our deposition system. The morphological properties of this type of coatings deposited by sputtering under similar conditions have been extensively studied, and information can be found in the literature [20–22].

The double silver coating [23] (Ariño Duglass Dag66™) contains three different materials in seven layers: two layers of *Ag*, three layers of SnO_2 interspersed between them to protect them, and two layers of *NiCr* to prevent the oxidation of silver when depositing tin oxide. The composition from the substrate up and its manufacturing characteristics are defined in Table 1 The thickness of the layer is calibrated using a profilometer (see section 2.3).

Chemical	Thickness (nm)	Ar (sccm)	O_2 (sccm)	Power (W/cm^2)
SnO_2	34	150	180	3.00
NiCr	1	300	-	0.42
Ag	14	300	-	0.83
SnO_2	77	150	180	3.00
NiCr	1	300	-	0.42
Ag	10	300	-	0.83
SnO_2	29	150	180	3.00

Table 1: Low emissive coating structure of double silver (Dag66). The thickness determination error is around 5%.

2.2 Laser ablation

The next step is the selective removal of the coating by laser ablation to define the FSS. Laser radiation is absorbed by the coating material, which sublimates or evaporates and can even transform into plasma.

There is ample previous work dedicated to the optimization of the engraved FSS patterns. We start with a simple grid of horizontal and vertical lines, with 0.1mm line thickness and 1mm line spacing. 5 and 10mm spacing will also be used later.

As we can see in Figure 2, this capacitive FSS will work as a low-pass filter for a wave with an electric field linearly polarized in the direction normal to the lines. Another set of lines, perpendicular to the first one, will define a similar FSS for the other linear polarization.

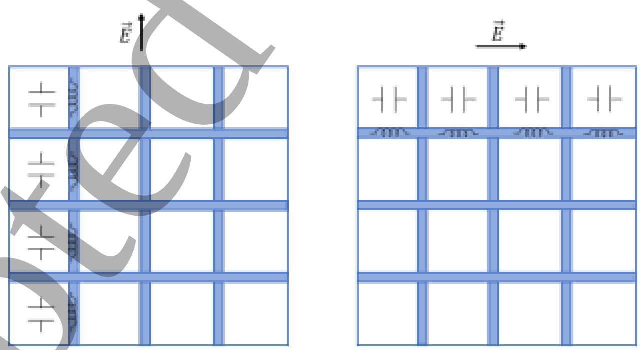

Figure 2: FSS high pass mesh with its equivalent elements.

Laser ablation of the coating is performed using a 35W 1064nm Rofin Powerline 6 solid state Nd:YAG laser. By adapting a 254mm focal length lens, we can work with the 300x300 mm glass samples with the low-e metallic coating.

There is literature on the effect of a pulsed laser on a thin metallic layer[24][25]. In this work, we have used a laser of nanosecond pulse duration (100ns) [26]. Therefore, the dominant effect we have found is material melting. On the other hand, the distribution of heat depends both on the metallic layer and on the substrate where it is deposited. In our work, the silver layers are surrounded by layers of SnO_2 and on a glass substrate, with low thermal conductivity, so the heat will not permeate the substrate.

The parameters to take into account are the intensity of the current applied to the laser, its modulation frequency and the speed of the beam movement. These last two parameters define the firing speed and thus the resolution of the ablation in points per inch. These three parameters define whether a total or partial removal of the coating material is obtained. To calibrate it, a sweep of the different parameters of the laser has been performed.

2.3 Samples characterized

For the analysis of the properties of the samples, we used a visible and infrared spectrophotometer with a 350 to 2500nm wavelength range and 10nm steps, always in normal incidence of the beam on the sample. A Bruker Dektak XT stylus profilometer, a TIR 100-2 emissometer, and an OLYMPUS optical microscope. The wider layers (50-70 nm) have been deposited separately and subsequently measured with the profilometer, with an estimation of its standard error of 2 to 3 nm. Knowing the rate of deposition, we adjust the time to achieve the desired thickness, with a standard error of approximately 5% to adjust their deposition time. The NiCr layer has the minimum thickness necessary, experimentally determined, to avoid oxidation of the silver.”

The samples were also characterized by Field Emission Scanning Electron Microscopy (FESEM), which allows us to measure with up to 0.8 nm of spatial resolution, using an acceleration voltage between 0.02kV and 30kV. Sample images were taken at 3kV and 5kV EHT (primary-beam energy) with a working distance between 3 and 5mm. The probe current varies between 80 pA and 218 pA and the energy selective backscattered (EsB) grid voltage is 1.5 kV. We also used an EDS (Energy Dispersive Spectroscopy) detector for scattered x-ray energy analysis and a vacuum control system. In our case, we will use a 5kV silicon and 15kV cobalt standard as a reference.

This device allows us to take micrometric images of the sample and analyse its chemical composition, to check the changes that the laser has made in the metallic layer.

A waveguide setup was also used to measure the microwave transmission of the samples (Figure 3).

Figure 3: Waveguide setup to measure microwave transmission through glass.

3. Theory model

3.1 FSS on glazing circuit model

The most common and basic frequency selective surface is a capacitive low pass filter, defined by the removal of a set of parallel lines forming a grid [27]. If the E-field of the electromagnetic wave is perpendicular to the lines, the remaining conductive areas act as capacitors, and the narrower the gap between conductors, the greater the equivalent capacitance. This FSS can be made polarization independent by defining another set of lines perpendicular to the first one.

To achieve maximum transmittance at RF frequencies we must raise the cutoff frequency of the filter, by making the equivalent capacitor smaller, until we allow the higher frequency needed (usually in the 5-10 GHz range) to pass unimpeded.

On the other hand, this filter will continue to block frequencies such as those of infrared light, which are much higher (in the order of hundreds of THz). The loss of effectiveness of the low-e coating will simply be proportional to the ratio of the total surface removed. The difference of almost five orders of magnitude between those two frequency ranges gives an ample security margin to the definition of the cutoff frequency of the filter.

The fundamental point is the relationship between thickness and line distance. There are several settings that delimit the RF frequency range that is filtered by the frame structure. We are going to use the equivalent circuit theory of N.Marcuvitz [28], with the addition of a transmission line model for the glass sample [29].

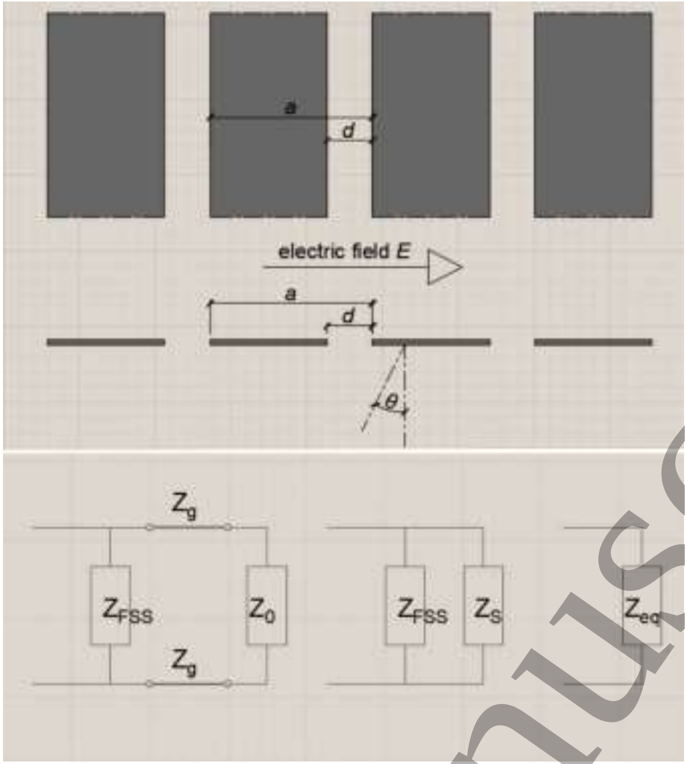

Figure 4: a capacitive grid (up), and equivalent circuit (down).

A capacitive grid of zero thickness is defined by two parameters (Figure 4 up): the thickness of the lines without metal (d), the distance between these lines (a). We also need the angle of incidence (θ) and the wavelength (λ). The normalized susceptance of a capacitive patch FSS will then be:

$$\frac{B}{Y_0} = \frac{4\boldsymbol{a}\cos\boldsymbol{\theta}}{\boldsymbol{\lambda}}\left\{ln\left(csc\left(\frac{\pi\boldsymbol{d}}{2\boldsymbol{a}}\right)\right) + \frac{1}{2}\left(\frac{(1-\alpha^2)^2\left[\left(1-\frac{\alpha^2}{4}\right)(A_+ + A_-) + 4\alpha^2 A_+ A_-\right]}{\left(1-\frac{\alpha^2}{4}\right) + \alpha^2\left(1+\frac{\alpha^2}{2}-\frac{\alpha^4}{8}\right)(A_+ + A_-) + s\alpha^6 A_+ A_-}\right)\right\} \quad (1)$$

Where

$$\alpha = \sin\frac{\pi\boldsymbol{d}}{2\boldsymbol{a}} \quad (2) \quad and \quad A_-^+ = \frac{1}{\sqrt{1 \pm \frac{2\boldsymbol{a}}{\boldsymbol{\lambda}}\sin\boldsymbol{\theta} - \left(\frac{\boldsymbol{a}\cos\boldsymbol{\theta}}{\boldsymbol{\lambda}}\right)^2}} - 1 \quad (3)$$

Thus, the FSS is equivalent to a capacitor, and the glass substrate can me modelled as a transmission line section of impedance Z_g and length l_g equal to the substrate thickness.

As the measurement is going to be performed in a rectangular waveguide setup of dimensions *axb*, the impedance Z_g will be the impedance of the fundamental TE_{10} mode of the waveguide filled with glass. The line will be terminated with a load of impedance Z_0, the TE_{10} mode impedance of the waveguide filled with air (Figure 4 down):

$$Z_g = \frac{1}{\sqrt{1-\left(\frac{f_{cg}}{f}\right)^2}}\eta_g; \qquad Z_0 = \frac{1}{\sqrt{1-\left(\frac{f_{c0}}{f}\right)^2}}\eta_0$$

Where f_{cg} and f_{c0} are the TE_{10} mode cutoff frequencies for a glass and air-filled waveguides, $\frac{v}{2a}$, and η is the intrinsic impedance of glass and air.

From the equivalent impedance of this circuit, Z_{eq}, we can evaluate the reflection coefficient of the sample,

$$\Gamma = \frac{Z_{eq} - Z_0}{Z_{eq} + Z_0}$$

And its transmission coefficient,

$$T = 1 - |\Gamma|^2$$

3.2 Optical and thermal properties.

Another important point is the spectral measurement in the optical range, to look for degradation in performance of the low-e coating. The solar reflectance and transmittance are obtained by weighting the spectral reflectance $R(\lambda)$ of a sample with a representative solar spectrum $S(\lambda)$. Illuminant D65 is generally used [30].

$$T_{solar} = \frac{\int_{350}^{2500} T(\lambda)S(\lambda)d\lambda}{\int_{350}^{2500} S(\lambda)d\lambda}; \quad R_{solar} = \frac{\int_{350}^{2500} R(\lambda)S(\lambda)d\lambda}{\int_{350}^{2500} S(\lambda)d\lambda} \quad (17)$$

The energetic properties of glass are unified in the thermal transmission coefficient U [31].

$$\frac{1}{U} = \frac{1}{h_e} + \frac{1}{h_t} + \frac{1}{h_i} \quad (18)$$

When external heat transfer coefficient h_e=23, h_t is the total thermal conductance of the glazing. Also internal heat transfer coefficient,

$$h_i = 3.6 + \frac{4.4\varepsilon}{0.837} \quad (19)$$

The emissivity ε of the sample is obtained from reflection measurements at thirty specific wavelengths in the infrared [31].

4. Results and discussion

4.1. Field emission Scanning Microscopy

In order to study the best parameters of the laser to obtain the cleanest lines possible, we have performed a morphological and structural characterization by Field Emission Scanning Electron Microscopy (FESEM).

The design of the engraving consists of a 1x1mm grid (Figure 5), generated by a 100-µm-wide laser beam incident on our 200-nm-thick multilayer coating deposited on a glass substrate.

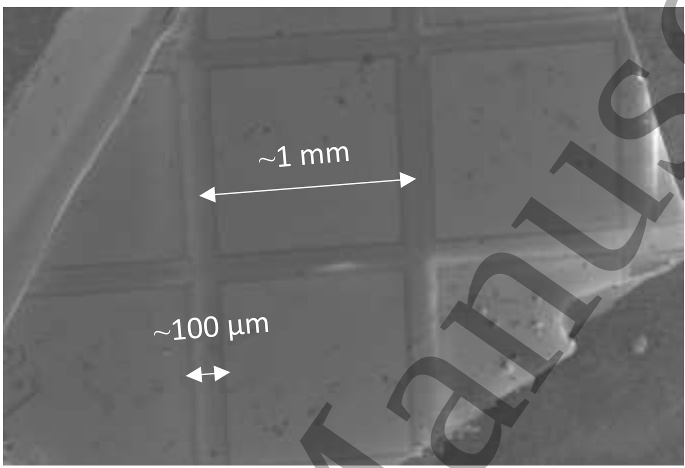

Figure 5: Glass sample with laser marked coating x40.

We are interested in studying the remains left by the passage of the laser beam. In figure 6, the upper section (A) belongs to the intact coating, homogeneous and most of it formed by tin oxide. In the lower section of the figure (B), we can see the appearance of the sample after removing the coating with the laser.

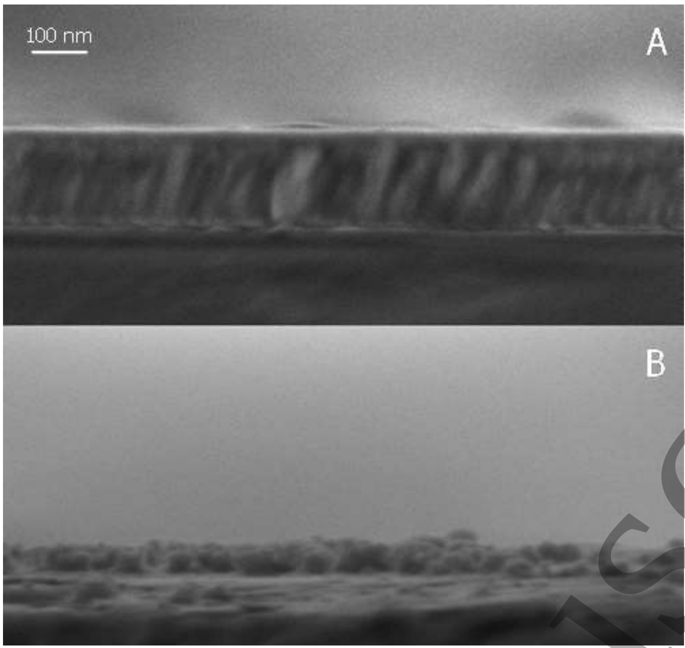

Figure 6: (A) intact coating, (B) coating removal.

Then we have analysed, using backscattering information, the area where the coating has been removed, in order to obtain information on the density of the material. In figure 7, we clearly distinguish the area of the bright and uniform metallic multilayer coating, but we can also observe residues from the coating around the area of ablation (right side of figure 7).

Figure 7: Beam incidence area using ESBx1000 signal.

We have also carried out a chemical analysis of the different areas of the sample. The chemical composition was done using a standard of cobalt (15 kV) and silicon (5 kV). As shown in figure 8, we have defined twenty-two areas to perform this analysis, in These areas can be grouped according to the incidence of the laser. In figure 9 we have one of the spectra by EDS measurements. In Table 2, we show the composition of the surface on the different areas.

Figure 8: Areas analysed in the sample.

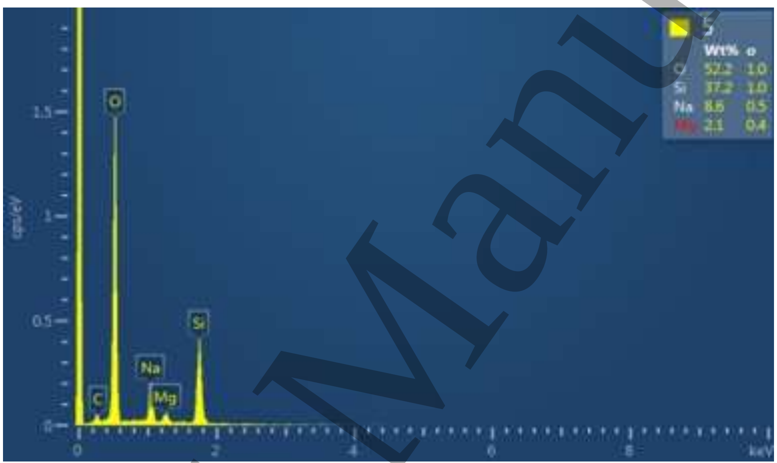

Figure 9: EDS spectrum of zone 5

Element	Zone	N	O	Na	Mg	Si	Ni	Ag	Sn
Glass	1		70.3	8.8	1.9	19.0			
Border laser	2		63.2	7.3	2.3	25.8	1.4		
	7	3.9	60.3	6.7	2.4	25.6	1.0		
	9	4.8	58.4	5.7	1.8	24.6	1.6	3.2	
	12		25.5			41.7		25.9	6.9
	20		33.6	4.9		41.5		14.6	5.4
	22		37.6	3.0	2.1	35.4	2.7	11.0	8.3
Centre laser	4		63.5	6.4	2.2	28.0			
	8	5.4	57.9	5.0	1.6	23.0	1.6	5.4	
	10	4.3	58.7	6.6	1.5	23.6		5.4	
	14		26.5			27.0		46.5	
	18		23.5			35.2		28.8	12.5
	19		27.1			39.4		33.6	
	21		33.5	3.9		31.2		18.9	12.5
Metallic	3		49.7				3.7	21.2	25.5
	6		60.0				4.5	11.1	24.4
	11		59.7				4.2	11.4	24.8
	13		53.3	4.0				42.7	0
Second	5		64.7	7.4	1.7	26.3			
	15		34.1	6.4	2.6	56.9			
	16		29.0	5.5	3.9	61.6			
	17		33.9	6.4	2.1	57.6			

Table 2: Proportion of chemical elements detected in the samples

The first area, Zone 1, belongs to the bare glass substrate without coating. It will be used as a reference of a clean laser ablation.

Zones 3, 6, 11 and 13 represent the areas with an intact coating, and as expected Ni, Ag and Sn, the elements that make up the multilayer, are detected in large quantities.

Zones 2, 7, 9, 12, 20, y 22 are the line edges. Glass elements are detectable, as well as the metallic elements that form the coating. Probably the glass and the coating have fused together in these areas.

Zones 4, 8, 10, 14, 18, 19 and 21 belong to the centre of the laser path. Here, remnants from the coating are also detected.

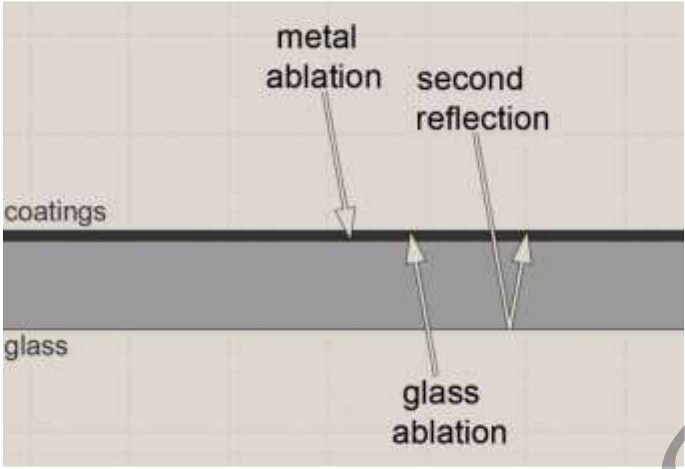

Figure 10: Types of laser incidence on the samples.

Finally, zones 5, 15, 16 and 17 contain marks due to a secondary ablation, after the laser is reflected on the glass second face (see figure 9). Their chemical composition is similar to that of bare glass. It is known that film side irradiation has different ablation results that glass substrate side irradiation [26]. These ablation conditions seem to be optimal; this indicates that striking from the opposite side (glass ablation in figure 9) may be adequate to obtain a good ablation.

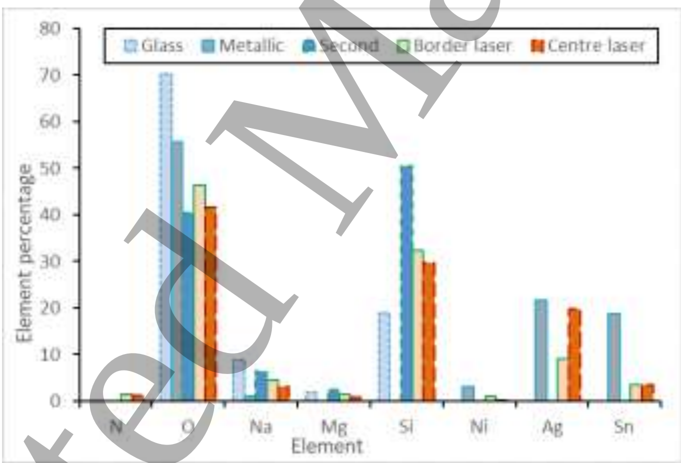

Figure 11: Percentage of each of the chemical elements in each of the areas analysed.

Figure 10 shows the results grouped by zone typology, and the weight percentage of each element present in each zone. The secondary ablation is the cleanest ablation, as it leaves nothing but Si and O (bare glass components). On the other hand, there are residues from the coating, Ag and Sn, both in the centre and the edge of the lines.

4.2. Contrast values

Now that we know the distribution of the ablation remnants on the substrate, it is necessary to define a method to measure the visual contrast between the multilayer and the ablation area. The mean squared error (MSE) of the intensity of the pixels of a microscope image will provide an estimation of the post ablation debris and will be related to the visual contrast of the lines engraved on the coating. We illuminate the sample by reflection to analyse the amount of light reflected by the sample.

First, we create a new image by the subtraction of an image of the intact coating to the image to analyse. Then we apply the MSE function to the intensities I_i of the pixels on that image.

$$MSE = \frac{1}{n}\sum_{i=1}^{n}\left(I_i - \hat{I}\right)^2 \qquad (20)$$

By applying this method to images taken with the same lighting conditions (Figure 11), we are able to establish an objective measure of the perceptibility of the FSS on a certain type of glass.

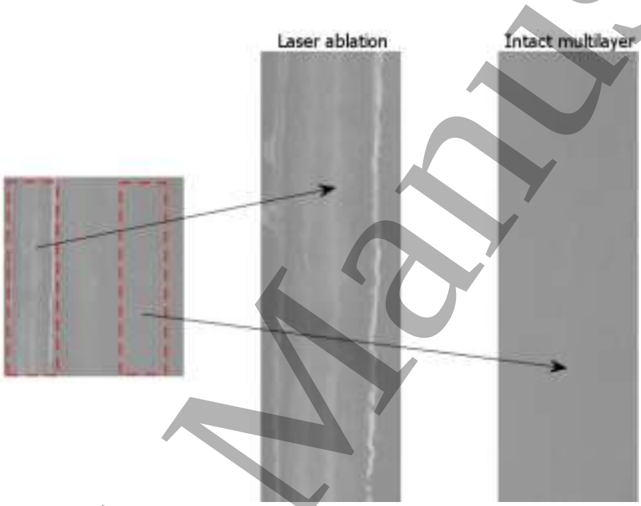

Figure 12: Application of the mean square error algorithm.

It is of crucial importance for the visual aspect of the glass to define the parameters of the laser beam with which we perform the ablation. To test our system, we have processed the images from different samples made with the GSI Lumonics Laser, using different power (28-32A) and frequency (1-5kHz) ranges.

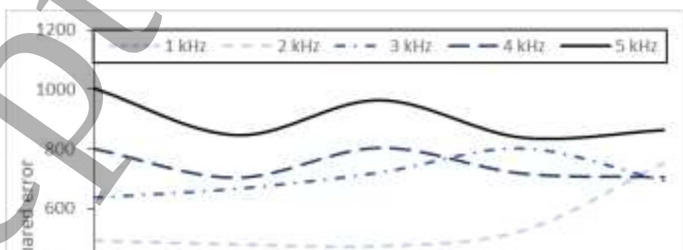

Figure 13: Application of the mean square error algorithm.

Figure 12 shows a clear increase in the mean square error with the frequency of the beam, but there is not a visible dependence with the laser power.

The laser ablation of the coating can be performed with the laser beam incident on the coated (metal ablation) or on the uncoated side of the glass substrate (glass ablation). In the previous section, we observed that the cleanest ablation happened with the second reflection of the laser, a configuration similar to the glass ablation.

We can use the MSE algorithm to the study of the differences between these two options (figure 9).

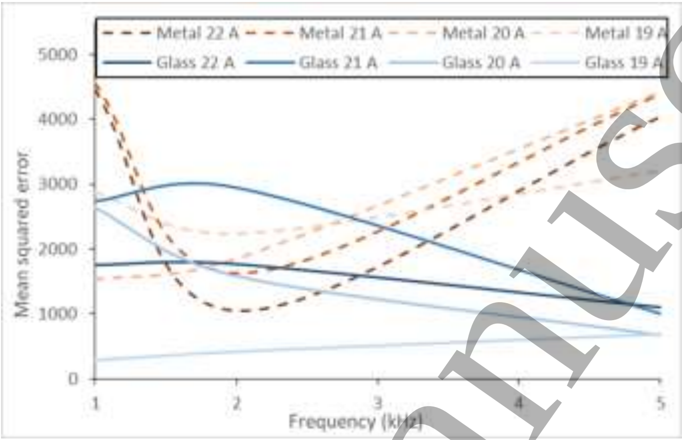

Figure 14: Application of the mean square error algorithm.

The sweep over the range of frequencies and laser currents shows two different behaviours (see figure 13), depending on the side used. When the laser is incident on the coated surface, there is a minimum of MSE around 2KHz, whereas optimum effect is achieved by striking the glass side with minimal intensity. The best (lower) values for MSE are obtained from the uncoated side, with a 19A laser current.

When the laser beam strikes directly on the coated side of the glass, the increase in frequency results in the apparition of reflecting metallic residues in the area of the removed layer. On the other hand, if the beam strikes in the uncoated side of the glass, passing through it before reaching the coating, the results are different. Thus, we conclude that the best configurations will always have the beam striking from the uncoated side of the glass.

As the coating total thickness is around 150 nm, a Buker Dektak XT profilometer has been used to ensure that the entire coating has been removed.

4.3. Optical and thermal properties and RF transmittance

Three different FSS samples, with 1, 5 and 10mm line spacing and 100-µm-thick lines, have been fabricated using the parameters defined in the previous section.

Line spacing is an important parameter. The smaller the size of the squares, the longer the processing time of the machine and the power consumed. Regardless of the laser design, there is an order of magnitude in the number of lines to be removed between the 1mm and 10mm squares. Also, railway windows must pass a strict photoenergetic regulation, so it is imperative to minimize the metallic surface removed from the glazing by the laser treatment. As a guideline, the processing of a 1300x800mm glass sheet using a line spacing of 7cm would take around 20 minutes in an industrial machine.

In figure 14, we can see the optical spectra of the original low-e coating glass and of the samples. All the samples maintain the optical characteristics of the original coating in the visible and near infrared range. Small differences in spectra are due to the difficulty of repeating exact thicknesses coatings.

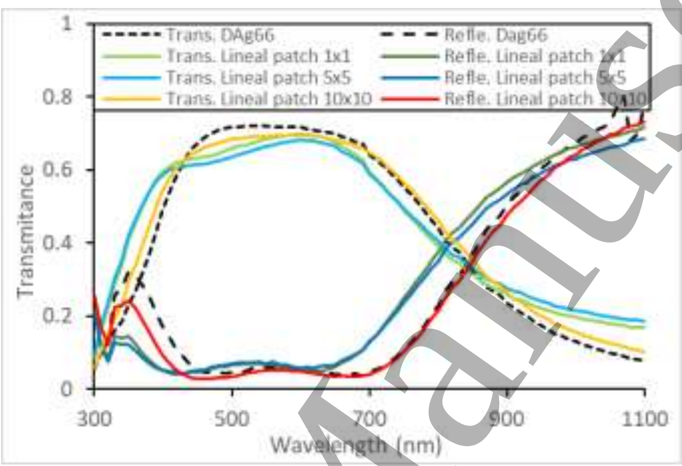

Figure 15: Spectral measure, original layer and with 1, 5 and 10 mm between lines.

On the other hand, to examine the thermal properties of the coating we must observe the infrared range, as the black body emission at 24ºC has its maximum at a wavelength around 10µm.

Figure 15 shows that the spectrum in the infrared does not stray far from that of the original coating and maintains the high reflectance properties of low-emissivity and solar control glasses. The only exception is the 1x1mm lineal patch, which suffers an appreciable decrease in reflectance. This is also consistent, as reflectance decreases as more coating surface is removed.

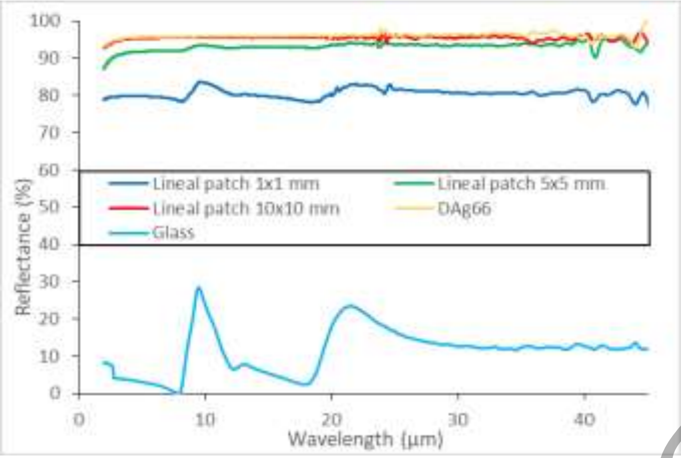

Figure 16: Spectral measure from 2 to 50 um of glass, original layer and with 1, 5 and 10 mm between lines.

With the reflection measurements in the infrared, we can calculate the emissivity of the samples [31]:

$$\epsilon_{Layer} = 0.06\,; \epsilon_{10x10} = 0.07\,;\ \epsilon_{5x5} = 0.09\,;\ \epsilon_{1x1} = 0.22\,;\ \epsilon_{Glass} = 0.83$$

From this, we can obtain the thermal transmission coefficient of the different samples (equations 18 and 19).

$$U_{Layer} = 3.3\ \ ; U_{10x10} = 3.4\ ;\ U_{5x5} = 3.4\,;\ U_{1x1} = 3.9\,;\ U_{Glass} = 5.8\ \frac{W}{m^2 \cdot K}$$

Comparing the calculated thermal transmittance coefficient of the FSS with that of the original layer, we confirm that the difference is barely 3%. Therefore, in most cases the FSS will hardly affect the performance of the structure as an energy efficient window.

We have also verified that the FSS defined with the parameters we have selected continue to work as intended. Again, we carried out the tests on our three FSS samples, with 1, 5 and 10mm line spacing.

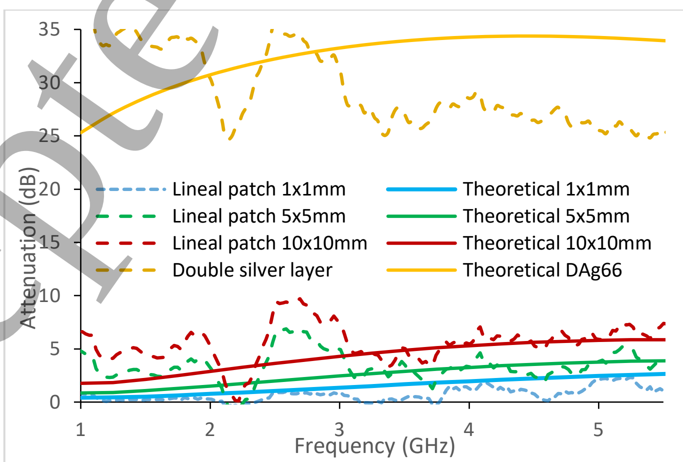

Figure 17: Radio frequencies attenuation of the FSS with 1, 5 and 10mm distance between lines. Theoretical versus waveguide measurement.

In figure 16 we show the attenuation of the different FSS and of the coated glass (double silver layer), both calculated and measured on the waveguide setup (dashed lines). All three samples achieve a great reduction in the RF attenuation of the low-e coating in the range of one to five gigahertz.

5. Conclusions.

In modern railcar windows, the optical properties of the low-e coatings used to reduce the heat transfer into or out of the vehicle are increasingly important. As far as we know, this is the first methodical and complete study that encompasses all the technical and aesthetic characteristics to take into account in this railway environment.

Our contrast evaluation method based on MSE is a useful tool to quantify the visual impact of the definition of FSS on low-e glazing. Using this method, we have found the optimal configuration parameters for our laser and determined that the best results are obtained when the beam is incident on the uncoated side of the glass. These parameters can obviously vary which each laser system, but are easily found with this algorithm.

Also, we have verified that, by removing the coating with the adequate laser current and frequency, we can improve the visual results without affecting the rest of the optical (visible), thermal (infrared) and communication (radio frequency) properties of the glazing.

For example, a 5x5mm grid will have a percentage of removed coating of **3.88%**, while the increase of the attenuation in the radio frequency range (more precisely between 1 and 5 GHz) due to the low-e coating will not reach **5dB**. Regarding the thermal properties of the glass (wavelengths between 2 and 50 μm in the infrared), the thermal transmission coefficient (U) only rises from **3.3 to 3.4W/m^{2}K**.

Acknowledgements.

Authors would like to acknowledge the use of Servicio General de Apoyo a la Investigation-SAI, Universidad de Zaragoza. This work has been funded by FEDER/Ministry of Science, Innovation and Universities Spanish State Research Agency (RTC-2017-6504-5) and by the collaboration between Ariño Duglass and the University of Zaragoza.

6. Bibliography

[1] B.P. Jelle, S.E. Kalnæs, T. Gao, Low-emissivity materials for building applications: A state-of-the-art review and future research perspectives, Energy and Buildings. 96 (2015) 329–356. https://doi.org/10.1016/j.enbuild.2015.03.024.

[2] C. Schaefer, G. Bräuer, J. Szczyrbowski, Low emissivity coatings on architectural glass, Surface and Coatings Technology. 93 (1997) 37–45. https://doi.org/10.1016/S0257-8972(97)00034-0.

[3] H.J. Gläser, Large Area Glass Coating .2005, (2005) 1–341.

[4] E. Ando, M. Miyazaki, Moisture resistance of the low-emissivity coatings with a layer structure of Al-doped ZnO/Ag/Al-doped ZnO, Thin Solid Films. 392 (2001) 289–293. https://doi.org/10.1016/S0040-6090(01)01045-8.

[5] J. Kulczyk-Malecka, P.J. Kelly, G. West, G.C.B. Clarke, J.A. Ridealgh, K.P. Almtoft, A.L. Greer, Z.H. Barber, Investigation of silver diffusion in TiO2/Ag/TiO2 coatings, Acta Materialia. 66 (2014) 396–404. https://doi.org/10.1016/j.actamat.2013.11.030.

[6] H.S. Roh, S.H. Cho, W.J. Lee, Study on the durability against heat in ITO/Ag-alloy/ITO transparent conductive multilayer system, Physica Status Solidi (A) Applications and Materials Science. 207 (2010) 1558–1562. https://doi.org/10.1002/pssa.200983769.

[7] J. Xamán, Y. Olazo-Gómez, I. Zavala-Guillén, I. Hernández-Pérez, J.O. Aguilar, J.F. Hinojosa, Thermal evaluation of a Room coupled with a Double Glazing Window with/without a solar control film for Mexico, Applied Thermal Engineering. 110 (2017) 805–820. https://doi.org/10.1016/j.applthermaleng.2016.08.156.

[8] K. Chiba, T. Takahashi, T. Kageyama, H. Oda, Low-emissivity coating of amorphous diamond-like carbon/Ag-alloy multilayer on glass, Applied Surface Science. 246 (2005) 48–51. https://doi.org/10.1016/j.apsusc.2004.10.046.

[9] H. Kim, S. Nam, Transmission Enhancement Methods for Low-Emissivity Glass at 5G mmWave Band, IEEE Antennas and Wireless Propagation Letters. 20 (2021) 108–112. https://doi.org/10.1109/LAWP.2020.3042524.

[10] O. Bouvard, M. Lanini, L. Burnier, R. Witte, B. Cuttat, A. Salvadè, A. Schüler, Structured transparent low emissivity coatings with high microwave transmission, Applied Physics A: Materials Science and Processing. 123 (2017) 1–10. https://doi.org/10.1007/s00339-016-0701-8.

[11] RAJ MITTRA CHI H. CHAN TOM CWIK, Techniques for analyzing frequency selective surfaces-a review - Proceedings of the IEEE, Proceedings of the IEEE. 76 (1988) 1593–1615.

[12] O. Bouvard, M. Lanini, L. Burnier, R. Witte, B. Cuttat, A. Salvadè, A. Schüler, Mobile communication through insulating windows: A new type of low emissivity coating, Energy Procedia. 122 (2017) 781–786. https://doi.org/10.1016/j.egypro.2017.07.396.

[13] R.S. Anwar, L. Mao, H. Ning, Frequency selective surfaces: A review, Applied Sciences (Switzerland). 8 (2018) 1–46. https://doi.org/10.3390/app8091689.

[14] Y.N. Picard, D.P. Adams, J.A. Palmer, S.M. Yalisove, Pulsed laser ignition of reactive multilayer films, Applied Physics Letters. 88 (2006) 23–25. https://doi.org/10.1063/1.2191952.

[15] M.C. Gupta, D.E. Carlson, Laser processing of materials for renewable energy applications, MRS Energy & Sustainability. 2 (2015) 1–15. https://doi.org/10.1557/mre.2015.3.

[16] I. Astrauskas, B. Považay, A. Baltuška, A. Pugžlys, Influence of 2.09-μm pulse duration on through-silicon laser ablation of thin metal coatings, Optics and Laser Technology. 133 (2021) 106535. https://doi.org/10.1016/j.optlastec.2020.106535.

[17] C. Loka, H.T. Yu, K.S. Lee, The preparation of thermally stable TiNx/Ag(Mo)/TiNx ultrathin films by magnetron sputtering, Thin Solid Films. 570 (2014) 178–182. https://doi.org/10.1016/j.tsf.2014.05.029.

[18] E. Carretero, R. Alonso, J.M. Marco, Oxygen diffusion at high temperatures within the SnO 2 /Sst interlayer in sputtered thin films, Applied Surface Science. 359 (2015) 669–675. https://doi.org/10.1016/j.apsusc.2015.10.160.

[19] P. Optiwhite, Low-iron clear float glass, (n.d.).

[20] M.A. Ruiz-Robles, N. Abundiz-Cisneros, C.E. Bender-Pérez, C.D. Gutiérrez-Lazos, A. Fundora-Cruz, F. Solis-Pomar, E. Pérez-Tijerina, New ultrathin film heterostructure for low-e application by sputtering technique: A theoretical and experimental study, Materials Research Express. 5 (2018). https://doi.org/10.1088/2053-1591/aab6a0.

[21] S.H. Yu, C.H. Jia, H.W. Zheng, L.H. Ding, W.F. Zhang, High quality transparent conductive SnO 2/Ag/SnO 2 tri-layer films deposited at room temperature by magnetron sputtering, Materials Letters. 85 (2012) 68–70. https://doi.org/10.1016/j.matlet.2012.06.108.

[22] R. Alvarez, J.C. González, J.P. Espinós, A.R. González-Elipe, A. Cueva, F. Villuendas, Growth of silver on ZnO and SnO 2 thin films intended for low emissivity applications, Applied Surface Science. 268 (2013) 507–515. https://doi.org/10.1016/j.apsusc.2012.12.156.

[23] A. Klöppel, B. Meyer, J. Trube, Influence of substrate temperature and sputtering atmosphere on electrical and optical properties of double silver layer systems, Thin Solid Films. 392 (2001) 311–314. https://doi.org/10.1016/S0040-6090(01)01049-5.

[24] B. Voisiat, M. Gedvilas, S. Indrišinas, G. Račiukaitis, Picosecond-laser 4-beam-interference ablation as a flexible tool for thin film microstructuring, in: Physics Procedia, Elsevier B.V., 2011: pp. 116–124. https://doi.org/10.1016/j.phpro.2011.03.113.

[25] F. Ruffino, M.G. Grimaldi, Nanostructuration of thin metal films by pulsed laser irradiations: A review, Nanomaterials. 9 (2019). https://doi.org/10.3390/nano9081133.

[26] M. Domke, L. Nobile, S. Rapp, S. Eiselen, J. Sotrop, H.P. Huber, M. Schmidt, Understanding thin film laser ablation: The role of the effective penetration depth and the film thickness, in: Physics Procedia, Elsevier B.V., 2014: pp. 1007–1014. https://doi.org/10.1016/j.phpro.2014.08.012.

[27] F. Costa, A. Monorchio, G. Manara, An overview of equivalent circuit modeling techniques of frequency selective surfaces and metasurfaces, Applied Computational Electromagnetics Society Journal. 29 (2014) 960–976.

[28] N. Marcuvitz, Waveguide Handbook, 1986. https://doi.org/10.1049/pbew021e.

[29] H. Oraizi, M. Afsahi, Analysis of planar dielectric multilayers as fss by Transmission Line Transfer Matrix Method (TLTMM), Progress in Electromagnetics Research. 74 (2007) 217–240. https://doi.org/10.2528/PIER07042401.

[30] ASTM International, G173-03(2012) Standard Tables for Reference Solar Spectral Irradiances: Direct Normal and Hemispherical on 37° Tilted Surface, 2012.

[31] AENOR, Glass in building. Determination of thermal transmittance (U value). Calculation method.pdf, 1997.